natureresearch
https://doi.org/10.1038/s41561-020-00666-0

Supplementary information

Deforestation-induced warming over tropical mountain regions regulated by elevation

In the format provided by the authors and unedited

Supplementary Information for

Deforestation-induced warming over tropical mountain regions regulated by elevation

Zhenzhong Zeng[1,2]*, Dashan Wang[1], Long Yang[3], Jie Wu[1,4], Alan D. Ziegler[5], Maofeng Liu[2], Philippe Ciais[6], Timothy D. Searchinger[7], Zong-Liang Yang[8], Deliang Chen[9], Anping Chen[10], Laurent Z. X. Li[11], Shilong Piao[12], David Taylor[13], Xitian Cai[14], Ming Pan[2], Liqing Peng[2], Peirong Lin[2], Drew Gower[2], Yu Feng[1], Chunmiao Zheng[1], Kaiyu Guan[15], Xu Lian[12], Tao Wang[16], Lang Wang[17], Su-Jong Jeong[18], Zhongwang Wei[19,20,21], Justin Sheffield[22], Kelly Caylor[23], Eric F. Wood[2]

[1] School of Environmental Science and Engineering, Southern University of Science and Technology, Shenzhen, China

[2] Department of Civil and Environmental Engineering, Princeton University, Princeton, NJ, USA

[3] School of Geography and Ocean Science, Nanjing University, Nanjing, China

[4] Department of Geoscience and Natural Resource Management, University of Copenhagen, Copenhagen, Denmark

[5] Faculty of Fisheries Technology and Aquatic Resources, Maejo University, Chiang Mai, Thailand

[6] Laboratoire des Sciences du Climat et de l'Environnement, CEA-CNRS-UVSQ, Gif-sur-Yvette, France

[7] Woodrow Wilson School, Princeton University, Princeton, NJ, USA

[8] Department of Geological Sciences, Jackson School of Geosciences, University of Texas at Austin, Austin, TX, USA

[9] Regional Climate Group, Department of Earth Sciences, University of Gothenburg, Gothenburg, Sweden

[10] Department of Biology, Colorado State University, Fort Collins, CO, USA

[11] Laboratoire de Météorologie Dynamique, Centre National de la Recherche Scientifique, Sorbonne Université, Ecole Normale Supérieure, Ecole Polytechnique, Paris, France

[12] Sino-French Institute for Earth System Science, College of Urban and Environmental Sciences, Peking University, Beijing, China

[13] Geography Department, National University of Singapore, Singapore, Singapore

[14] Climate and Ecosystem Sciences Division, Lawrence Berkeley National Laboratory, Berkeley, CA, USA

[15] Natural Resources and Environmental Sciences, University of Illinois at Urbana Champaign, Urbana, IL, USA

[16] Key Laboratory of Alpine Ecology and Biodiversity, Institute of Tibetan Plateau Research, Chinese Academy of Sciences, Beijing, China

[17] Department of Geography and Resource Management, The Chinese University of Hong Kong, Hong Kong, China

[18] Department of Environmental Planning, Graduate School of Environmental Studies, Seoul National University, Seoul, Republic of Korea

[19] River and Environmental Engineering Laboratory, Department of Civil Engineering, University of Tokyo, Tokyo, Japan

[20] Southern Marine Science and Engineering Guangdong Laboratory (Zhuhai), Zhuhai, China

[21] Guangdong Province Key Laboratory for Climate Change and Natural Disaster Studies, School of Atmospheric Sciences, Sun Yat-sen University, Guangzhou, China

[22] School of Geography and Environmental Sciences, University of Southampton, Southampton, UK

[23] Department of Geography, Bren School of Environmental Science & Management, University of California - Santa Barbara, Santa Barbara, CA, USA

*Correspondence to: zzeng@princeton.edu

Manuscript for *Nature Geoscience*

November 24, 2020

Contents of this file

Table S1. Overview of WRF configurations.

Domain	D1 (outer)	D2 (inner)
Dimensions (*x*, *y*)		
Southeast Asian Massif	220 × 175	190 × 190
Barisan Mountains in Maritime Southeast Asia	215 × 171	245 × 245
Serra da Espinhaco in South America	189 × 154	165 × 205
Albertine Rift mountains in Africa	179 × 139	140 × 205
Configurations		
Grid size (km)	25	5
Time steps (second)	60	60
Vertical layers	30	30
Physics		
Cumulus scheme	Kain-Fritsch scheme	Kain-Fritsch scheme
Microphysics scheme	WSM6	WSM6
Longwave radiation	RRTM scheme	RRTM scheme
Shortwave radiation	Dudhia scheme	Dudhia scheme
Surface layer	Monin-Obukhov scheme	Monin-Obukhov scheme
Land surface	Noah Mosaic, $N = 3$	Noah Mosaic, $N = 3$
Boundary layer	YSU	YSU

Table S2. The updated leaf area index (LAI) for different plant function types (PFT) for the tropics using the MODIS satellite observations.

Land cover type	Maximum LAI	Minimum LAI
Evergreen Needleleaf Forest	6.40	5.00
Evergreen Broadleaf Forest	5.92	4.83
Deciduous Needleleaf Forest	5.16	1.00
Deciduous Broadleaf Forest	4.03	0.71
Mixed Forests	5.23	2.30
Closed Shrublands	0.82	0.26
Open Shrublands	1.68	0.54
Woody Savannas	3.61	1.18
Savannas	2.55	1.07
Grasslands	1.19	0.73
Permanent Wetlands	1.50	1.13
Croplands	1.22	0.60
Urban and Built-Up	0.92	0.45
Cropland/Natural Vegetation Mosaic	1.81	0.77
Barren or Sparsely Vegetated	0.81	0.22

Figure S1. Satellite-observed forest loss and topography in the Southeast Asian Massif (SE1). (**a**) Spatial pattern of the forest cover change during 2000-2014 in hectares and percentage for each 5 km × 5 km (2500 hectares) grid cell: red, net forest loss; green, net forest gain. Dotting represents highlands (≥ 300 m). (**b**) Topography of the study region centered on Thailand (97.3° – 106.5° E, 12.1° – 20.7° N).

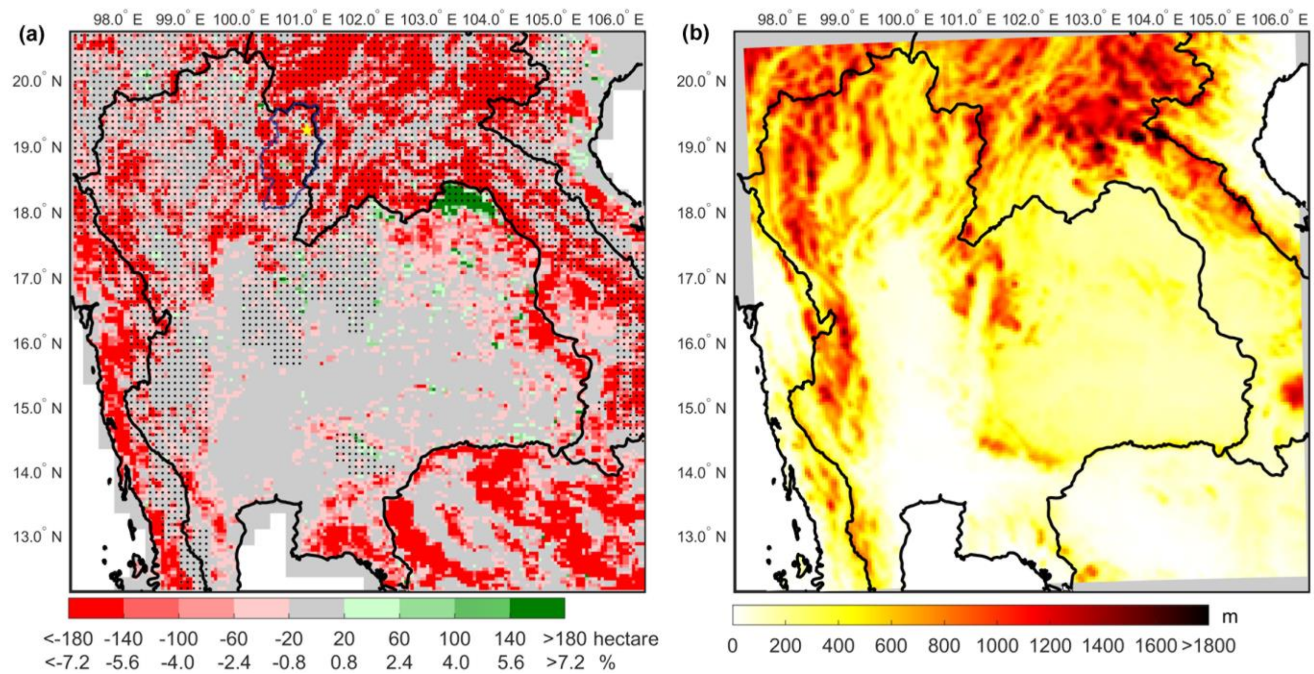

Figure S2. Satellite-observed forest loss at 5 km × 5 km grid cells and topography over three tropical mountain regions. (**a, d**) forest loss and topography in the Barisan Mountains in Maritime Southeast Asia (SE2). (**b, e**) forest loss and topography in the Serra da Espinhaco in South America (SA). (**c, f**) forest loss and topography in the Albertine Rift mountains in Africa (AF).

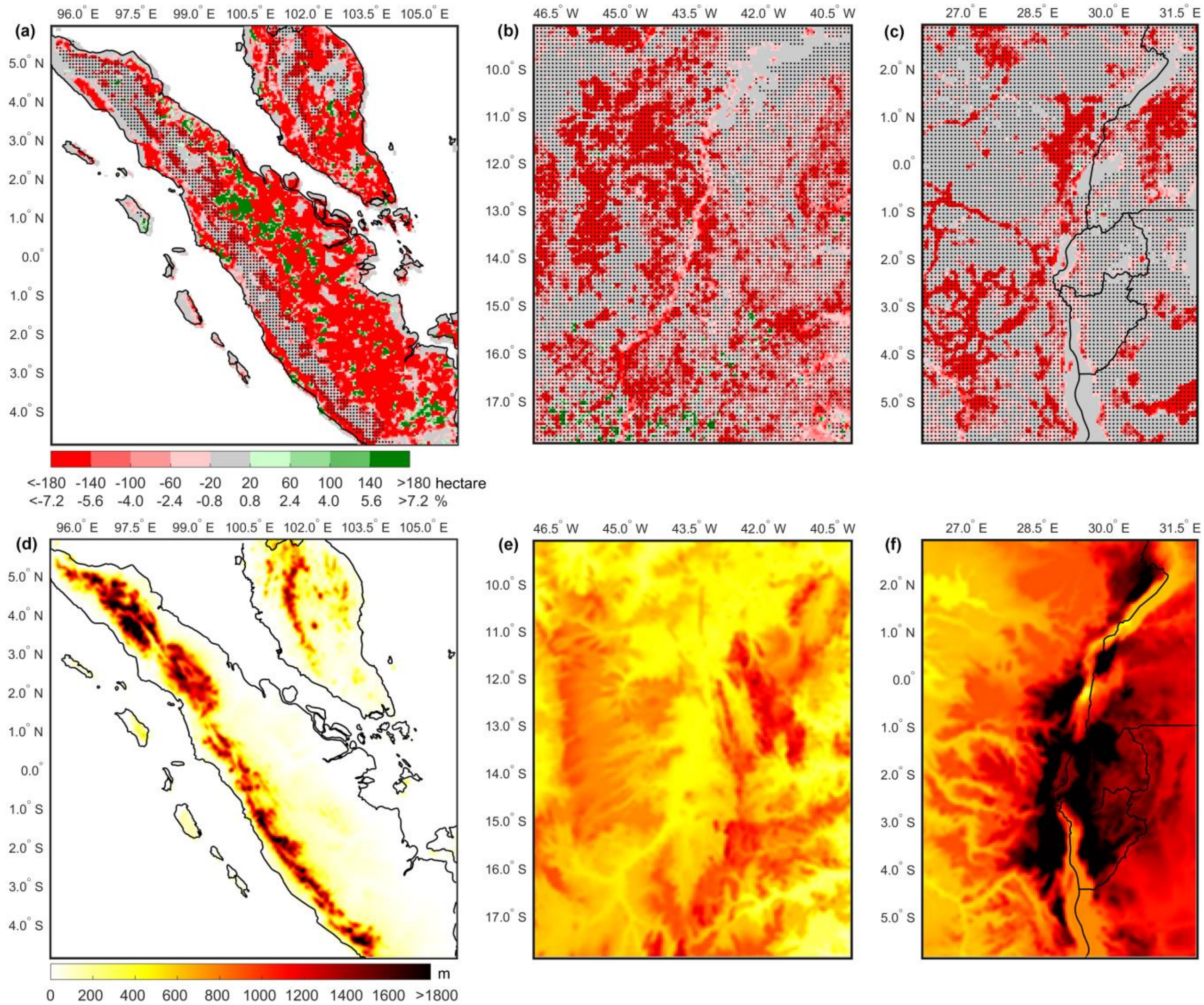

Figure S3. An example of the landscape of the upland cropland during the dry season (yellow star in Fig. S1a, a mountain village in Nan Province). The image was obtained from Google Earth (DigitalGlobe, 4/28/2019).

Figure S4. The WRF-Noah model grid meshes for the simulations over (a) SE1, (b) SE2, (c) SA, and (d) AF in this study. Each has two one-way nested domains, including the out-domain at a coarse grid spacing of 25 km (blue dots), and the inner-domain at a fine gird spacing of 5 km (red dots).

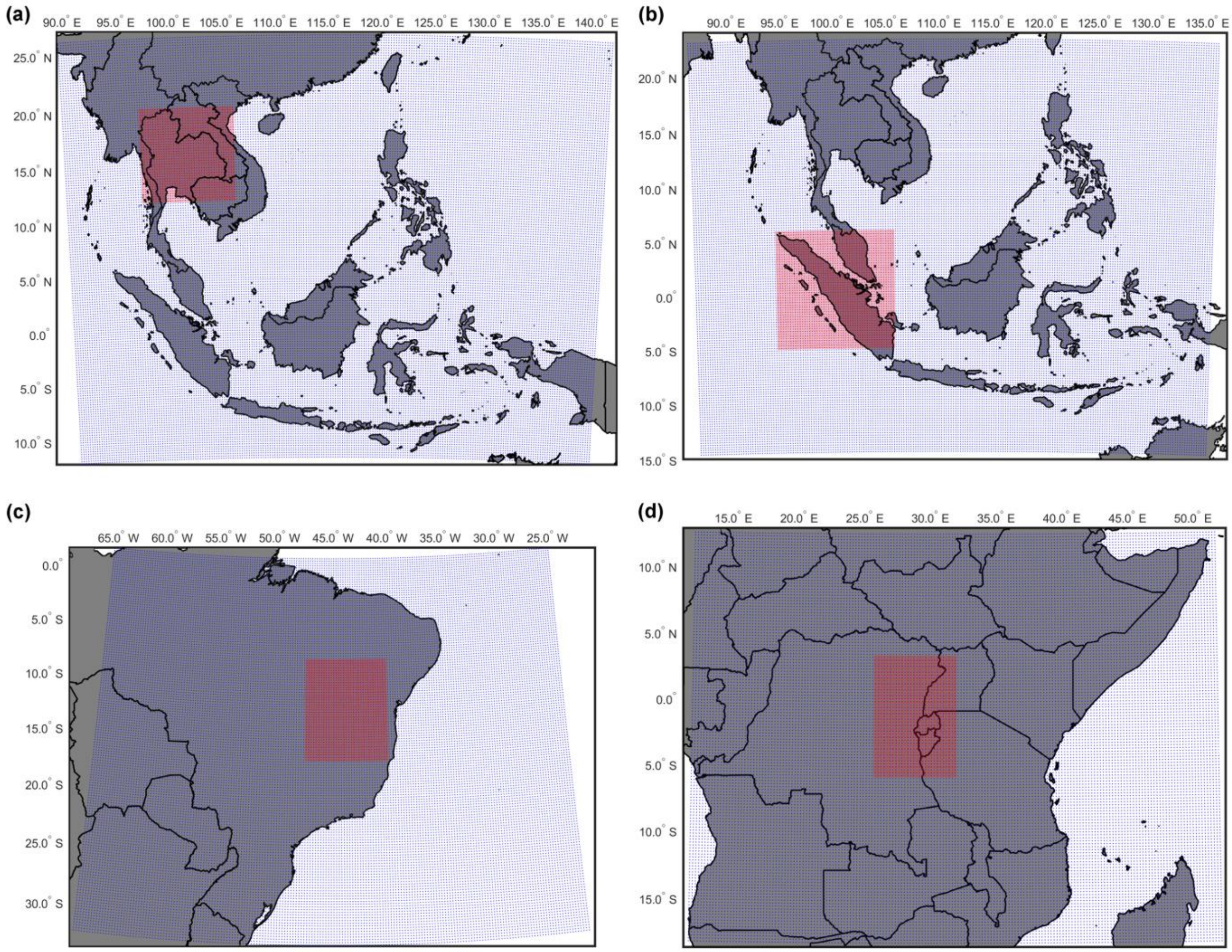

Figure S5. Validation on the modelled spatial-temporal variability of surface air temperature using 125 *in-situ* weather stations and the APHRODITE dataset in SE1. (**a**) Mean daily temperature averaged over the stations from 1 December, 2014 to 28 February, 2015. Black: temperature from the weather stations. Red: temperature from the WRF simulation using ERA5 reanalysis lateral boundary conditions. Blue: temperature from the WRF simulation using FNL reanalysis lateral boundary conditions. APHRODITE: temperature from the APHRODITE grid product. Inset numbers show the correlation coefficients and the *p*-values for the relations between the observation and the simulations (the product). (**b**) Simulated mean temperature versus the observed mean temperature in the stations averaged over the dry season. The inset plot shows the locations of the stations, 40 of the 125 stations are located in the highlands (> 300 m).

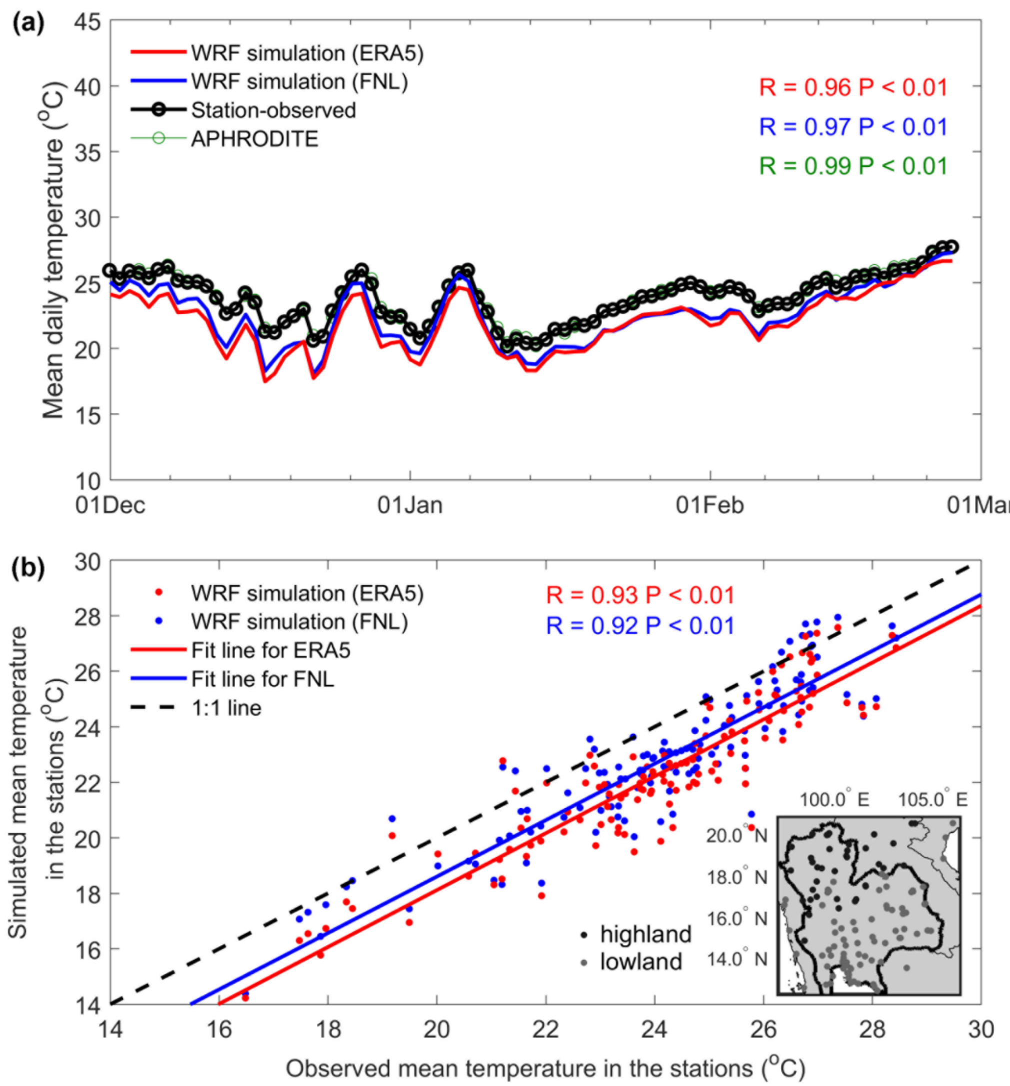

Figure S6. Validation on the modelled spatial-temporal variability of surface air temperature in the three tropical mountain regions. Mean daily temperature averaged over the *in-situ* stations for the dry season from 1 June to 31 August, 2014 over (**a**) SE2, (**b**) SA, and (**c**) AF. The total number of *in-situ* stations in the three mountain regions are 30, 5, and 9, respectively. Black: temperature from the weather stations. Red: temperature from the WRF simulation using ERA5 reanalysis lateral boundary conditions. APHRODITE: temperature from the APHRODITE grid product. Inset numbers show the correlation coefficients and the *p*-values for the relations between the observation and the simulations (the product).

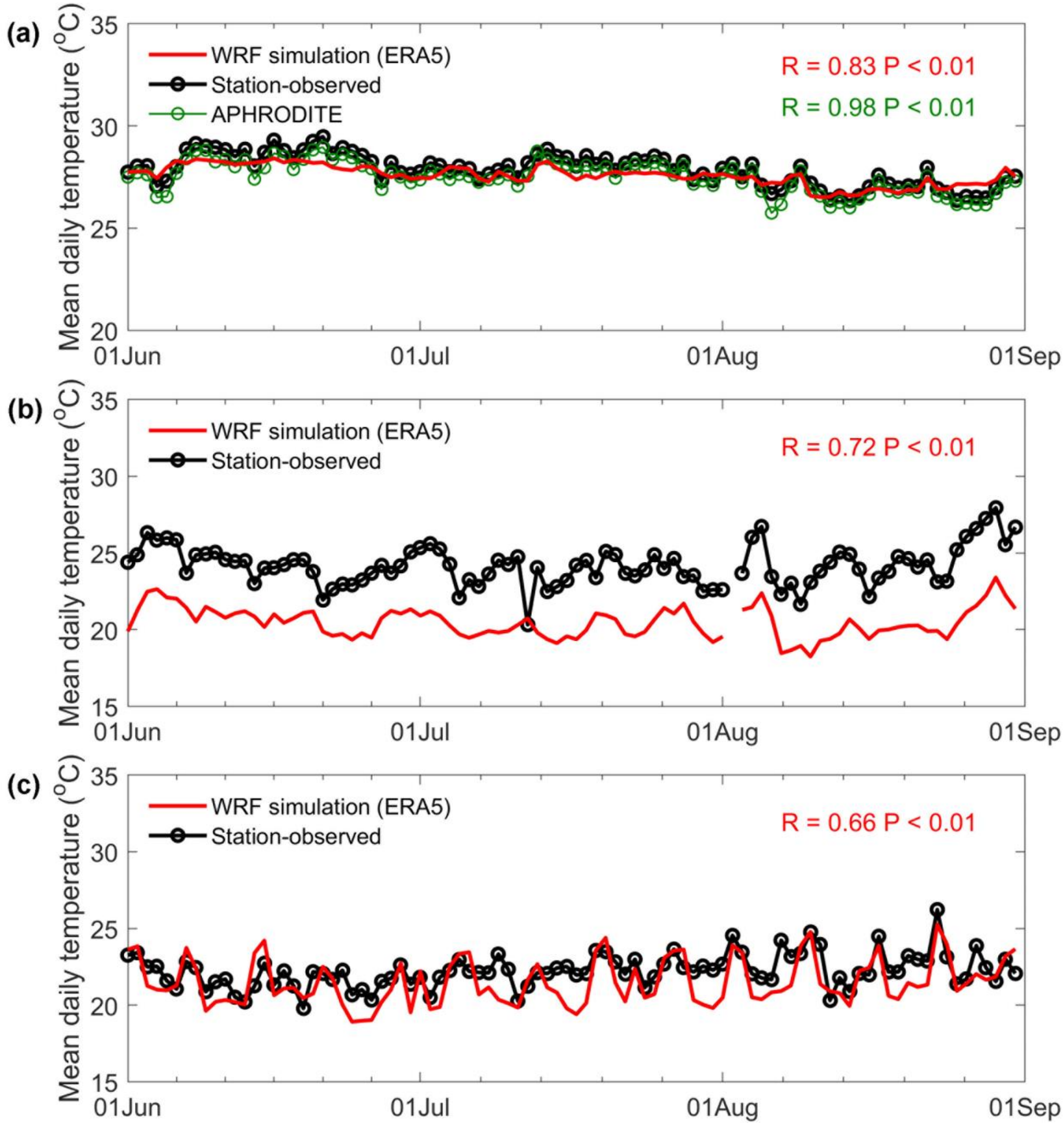

Figure S7. Reconstructed surface air temperature grounded on a dense of daily gauge data for Asia (a, APHRODITE) and model simulated surface air temperature (b, ERA5; c, FNL) over SE1 for the dry season from 1 December, 2014 to 28 February, 2015. The color within the white circles indicate the observed temperature from the 125 *in-situ* stations.

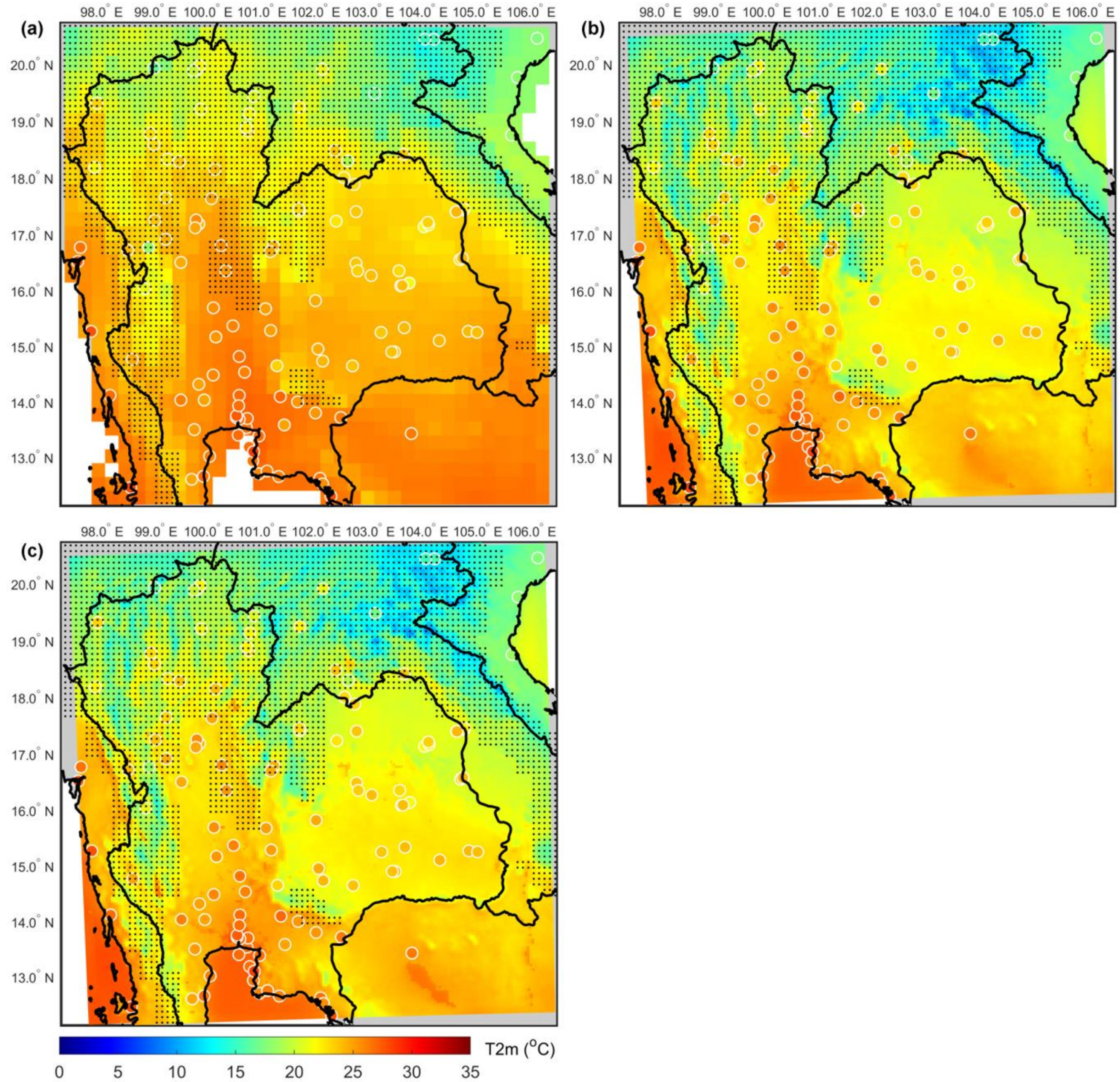

Figure S8. Gridded (a, APHRODITE) and model simulated (b, ERA5) surface air temperature over SE2 for the dry season from 1 June to 31 August, 2014. The color within the white circles indicate the observed temperature from the 30 *in-situ* stations.

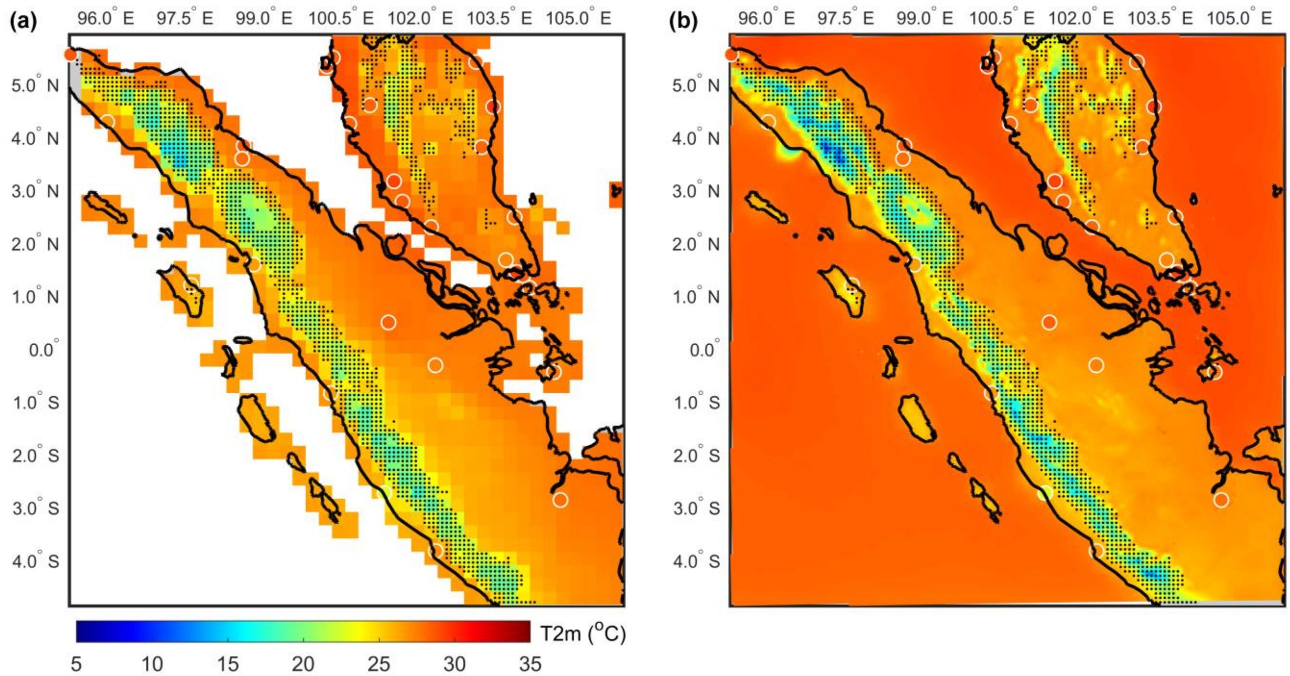

Figure S9. Boxplot of the temperature difference for a given grid cell (Longitude: 101.10 ºE; Latitude: 19.26 ºN) between the simulations with and without the observed forest cover change. In this grid (Fig. S3), 14.8% of the forest loss was occurred during 2000-2014. It is simulated to increase temperature by 0.17 ºC (95% confidence interval = 0.15–0.20 ºC; P < 0.01) during the dry season of 2014-2015. The inset numbers also include the results of the paired sample *t*-test. On the box, the central mark is the median, the edges of the box are the 25th and 75th percentiles, the whiskers extend to the most extreme data points not considered outliers, and outliers are plotted individually.

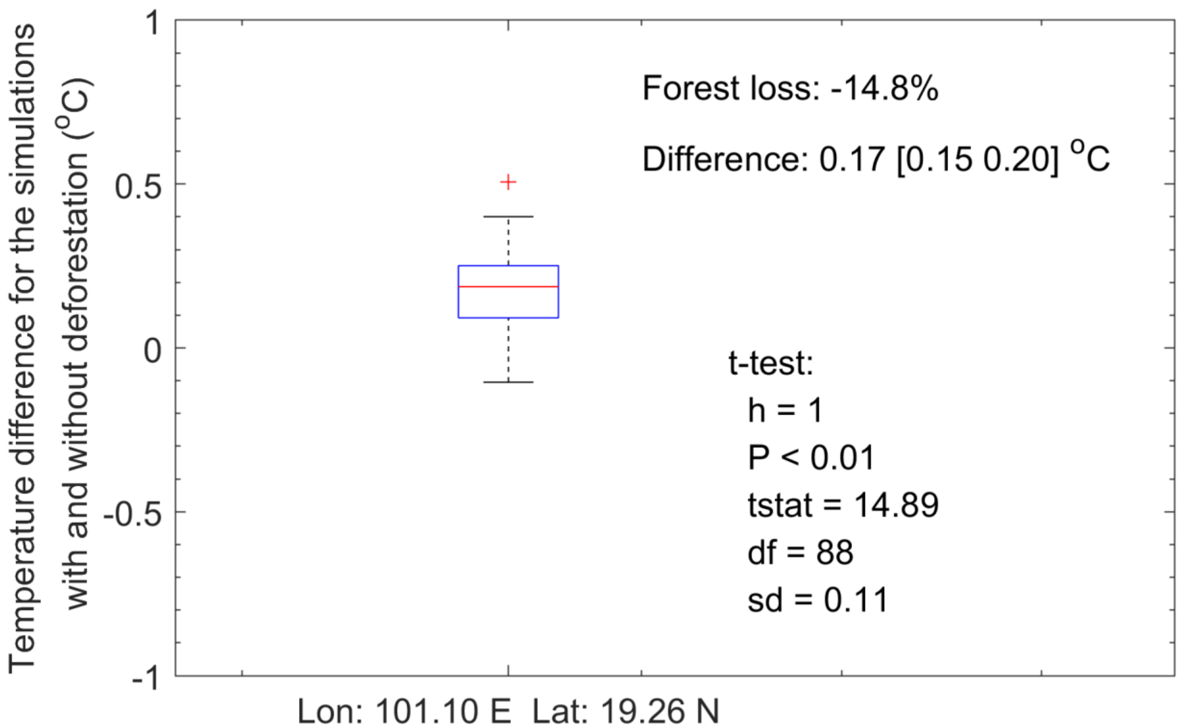

Figure S10. Sensitivity of albedo and evapotranspiration change to deforestation against elevation in (a, b) SE2, (c, d) SA, and (e, f) AF.

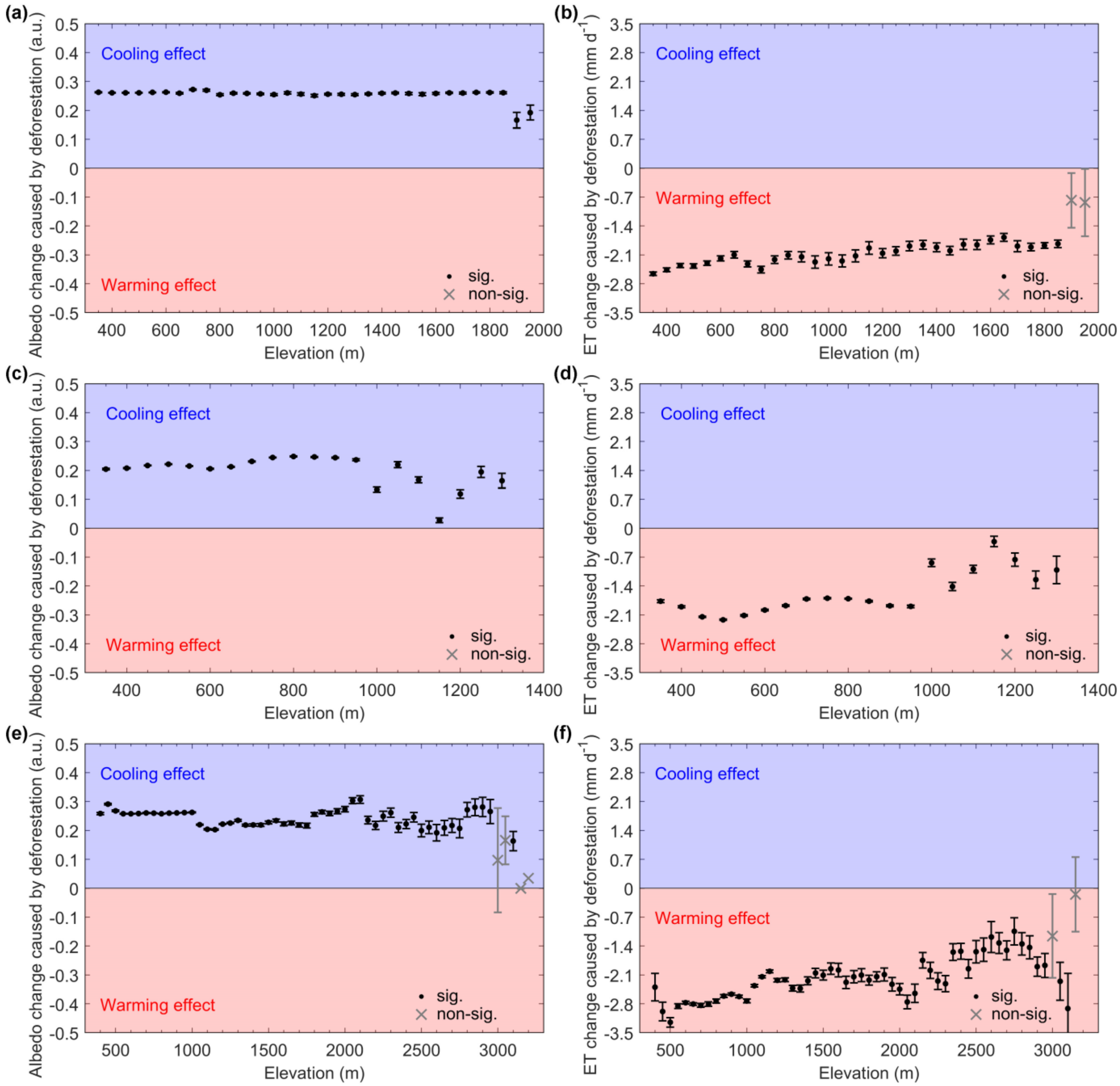

Figure S11. Elevational temperature gradient in the WRF simulations in the SE1. Red: WRF simulation using ERA5 reanalysis lateral boundary conditions. Blue: WRF simulation using FNL reanalysis lateral boundary conditions. Surface air temperature is simulated to decrease by 0.72 ºC with 100 m rise in elevation, like the observed gradient.

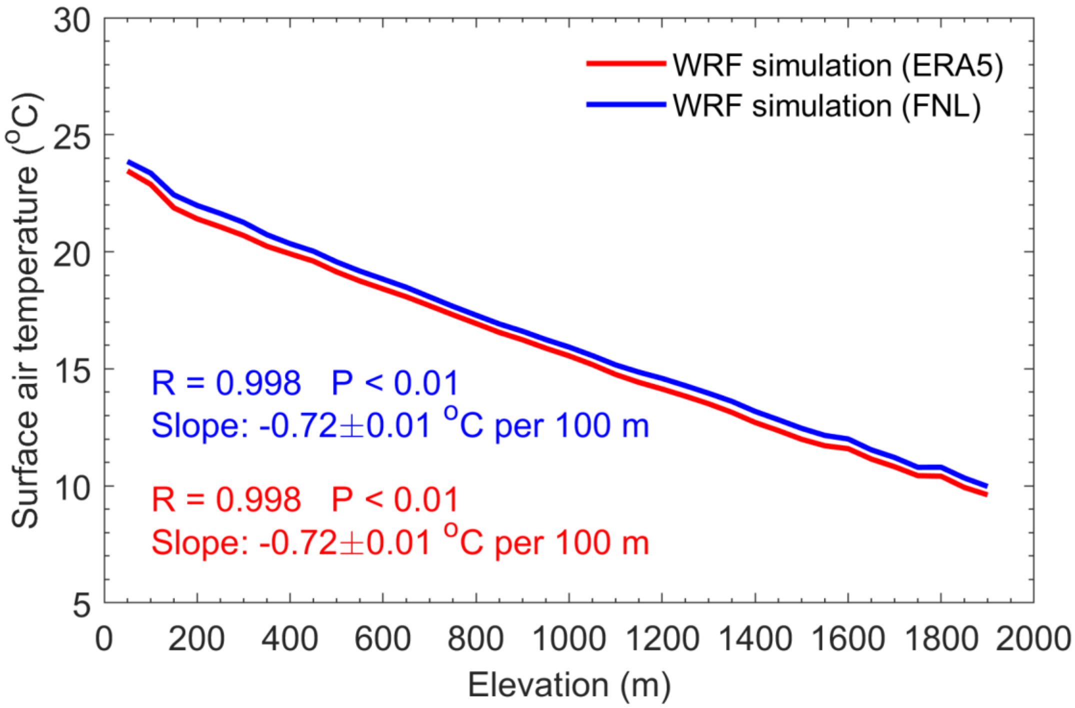

Figure S12. Same as Fig. 2a, but the temperature change at the grid level is calculated with the simulated daily temperature from 1 December to 28 February for the dry season of (a) 2012-2013, (b) 2013-2014, (c) 2015-2016, and (d) 2016-2017 over SE1.

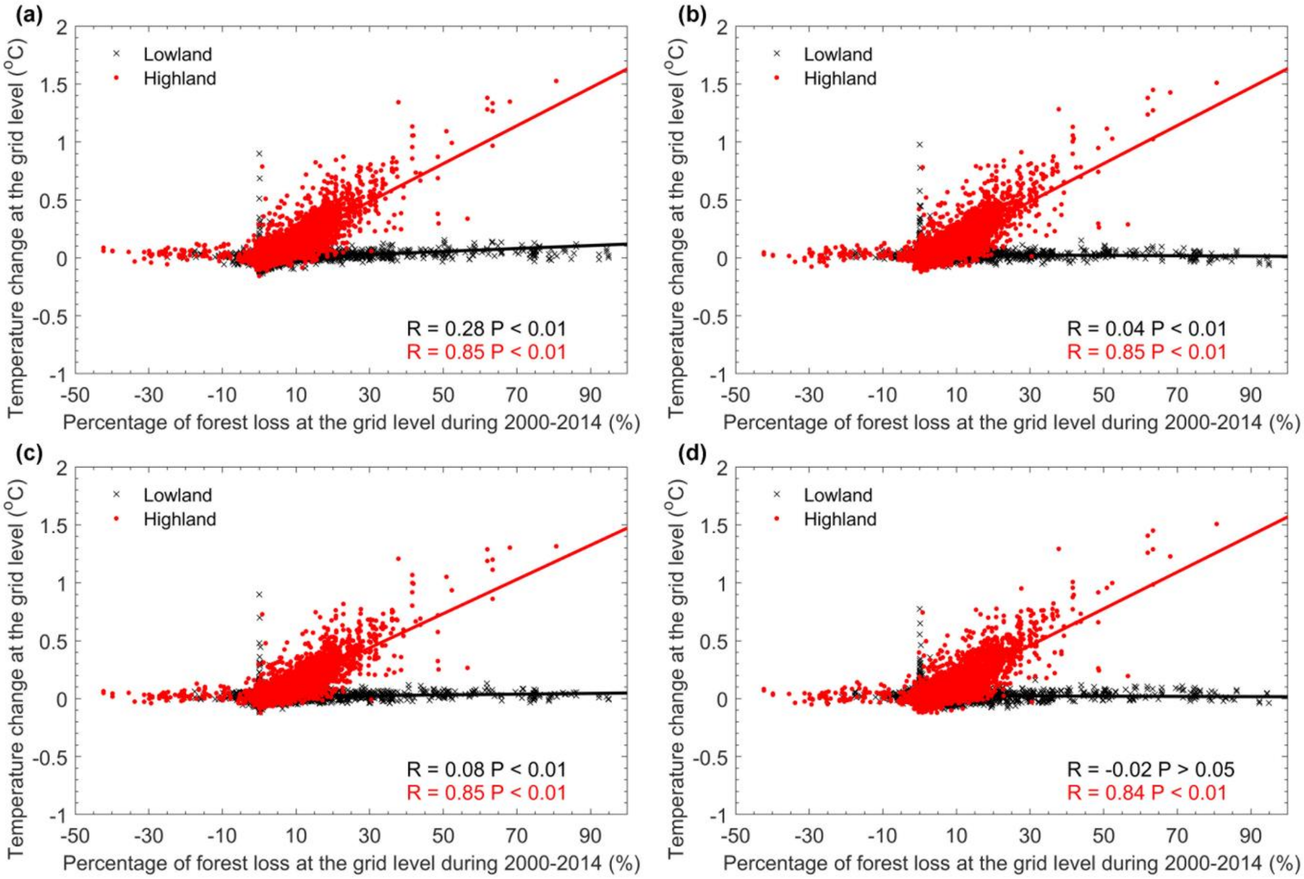

Figure S13. Same as Fig. 3a, but the temperature change at the grid level is calculated with the simulated daily temperature from 1 December to 28 February for the dry season of (a) 2012-2013, (b) 2013-2014, (c) 2015-2016, and (d) 2016-2017 over SE1.

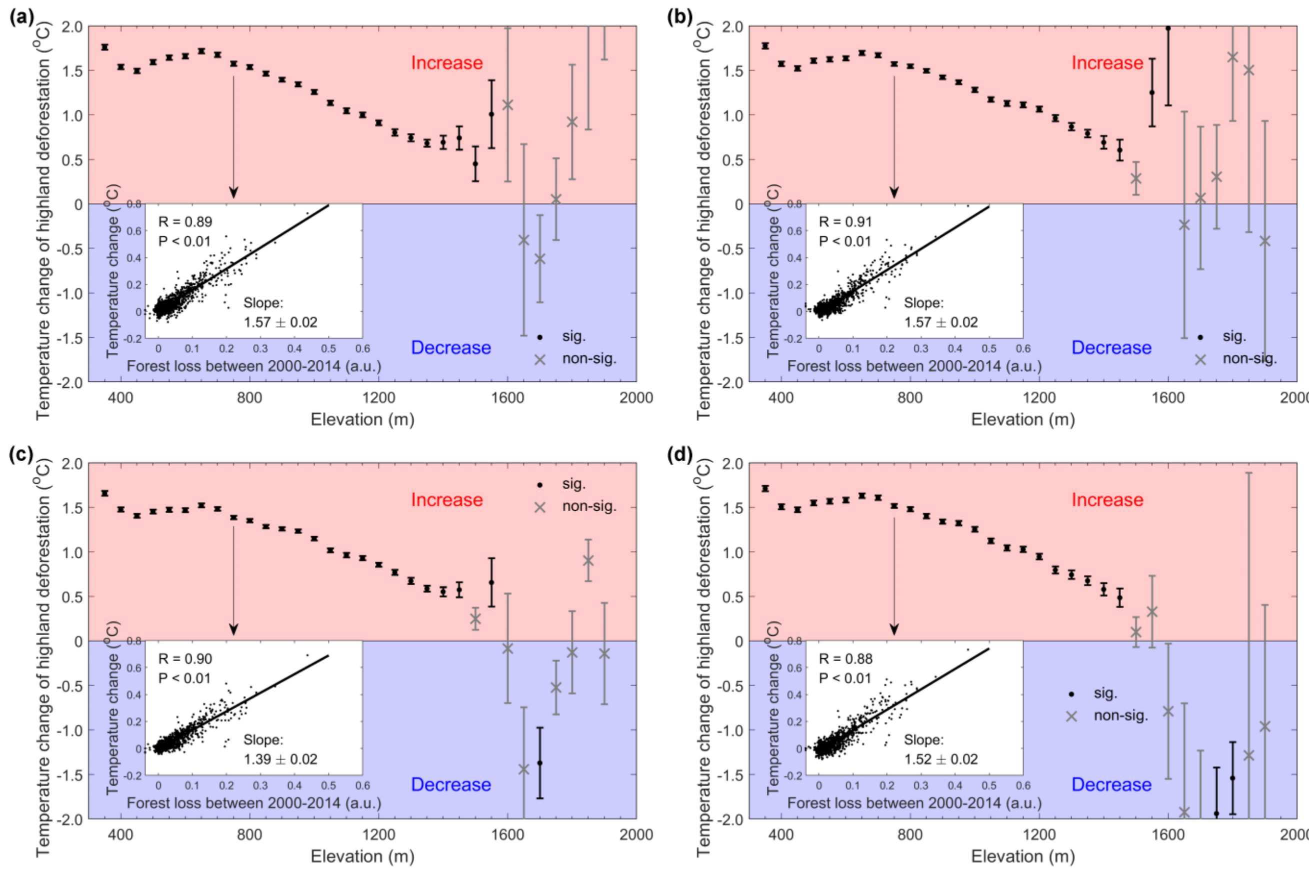

Figure S14. Same as Fig. 2a, but using the WRF simulations with FNL lateral boundary conditions.

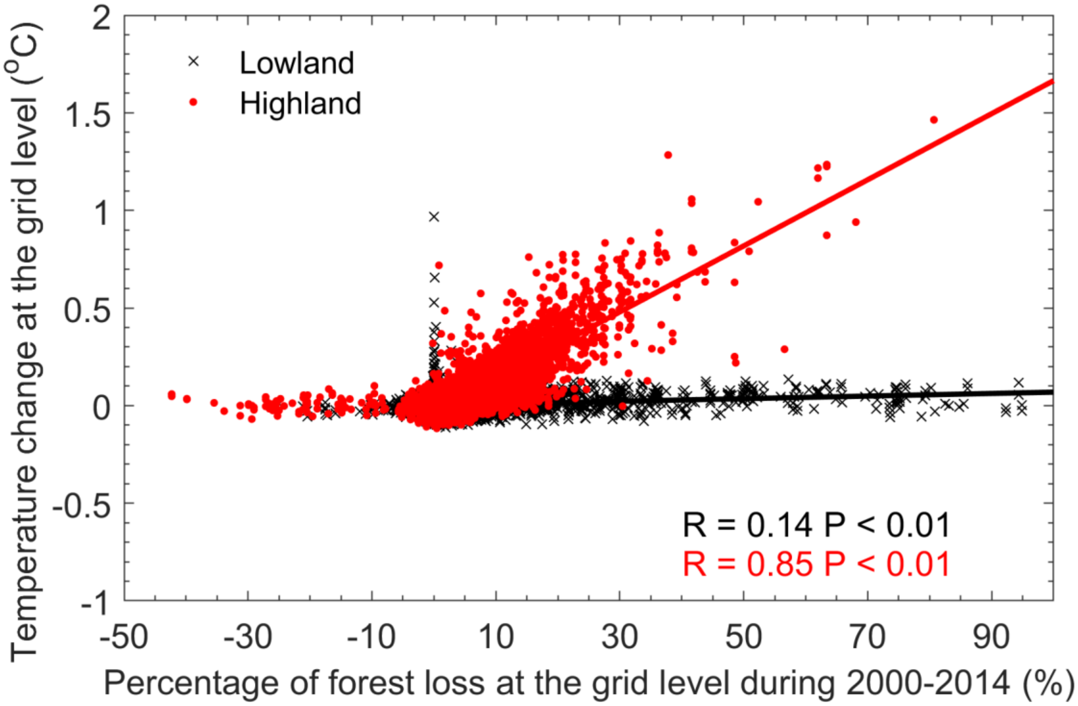

Figure S15. Same as Fig. 3a, but using the WRF simulations with FNL lateral boundary conditions.

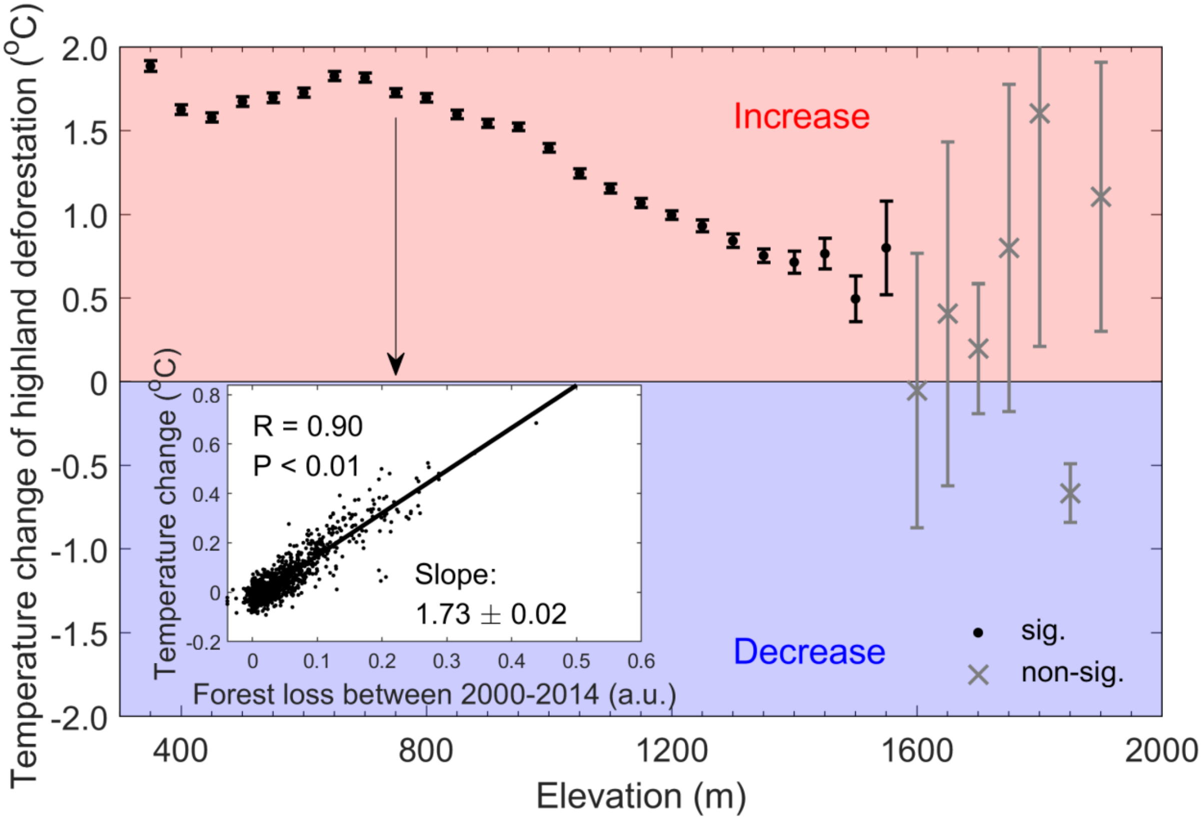

Figure S16. The simulated equivalent temperature (T_E) change under the cropland expansion-driven deforestation in SE1. (**a**) Same as Fig. 2a, but for the equivalent temperature change versus percentage of forest loss for 2000-2014 at the grid level. (**b**) Same as Fig. 3a, but for the regulation of elevation on the equivalent temperature change of highland deforestation. The equivalent temperature change at each grid cell is calculated with the simulated daily temperature from 1 December to 28 February for the dry season of 2014-2015.

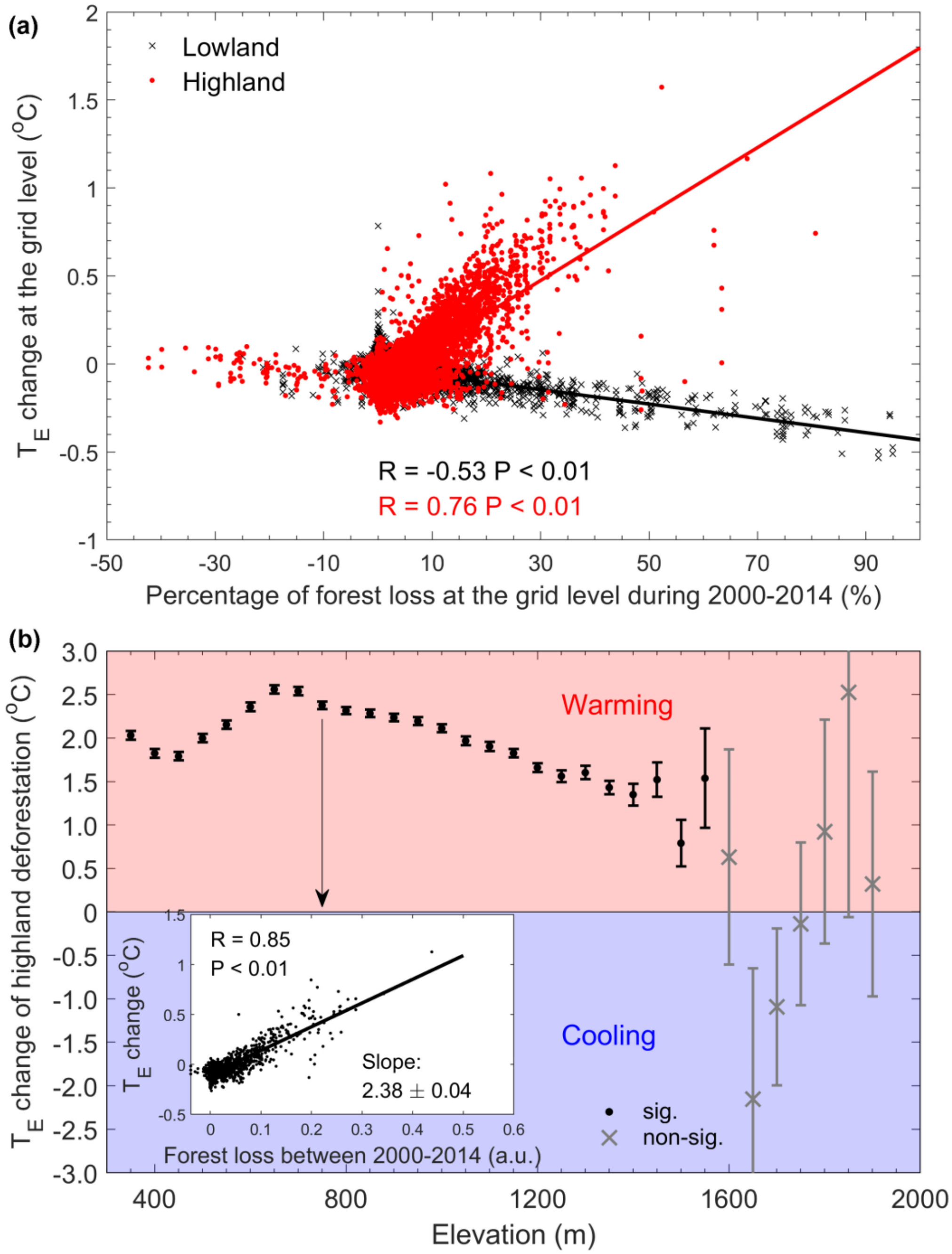

Figure S17. Topography, land use, the planning reservoirs in Nan Province, Thailand. Size of the black circles indicate the water storage capacity of the planning reservoirs. White lines are the rivers in the province. Dark red patches are the satellite-observed upland crops (mainly corn) for 2017. Yellow patches are the rice field. Purple patches are the perennial cropland. Black patches are the residence (town and villages). The background is the topographic map. The data is from private contacts with the local government.